Chapter 13
Inertial Sensors

Giorgio Allegato, Lorenzo Corso, and Carlo Valzasina

13.1 Inertial Sensors: An Historical Background

Inertial Sensors were one of the first product family developed using MEMS technology. The first paper about a MEMS accelerometer dates to 1979 when a bulk micromachined accelerometer was designed and first prototypes were manufactured at Stanford University [1]. Device working principle was based on piezoresistive sensing, and the MEMS structure was based on a glass-silicon-glass bonded wafer stack. Following this publication, it took about 20 years to have first MEMS accelerometers available on the market; the market driver for development was the replacement of switches for airbag deployment on automotive applications. In 1991, Analog Device commercialized the first industrial and high-volume MEMS accelerometer [2], realized by surface micromachining and based on capacitive sensing principle. About 10 years later, MEMS accelerometers from different suppliers entered the consumer market finding high-volume application in game consoles and expanding in the following years to smartphones, laptops, and IOT/wearable devices for more intuitive user interface and activity tracking.

As for the accelerometers, also MEMS gyroscopes required some decades from the first prototypes before achieving technology maturity for high-volume manufacturing. Driver application was still automotive for advanced safety systems for vehicle stability control.

G. Allegato · L. Corso
ST Microelectronics, Analog MEMS and Sensors Group, MEMS Technology and Design R&D, Agrate Brianza, Monza Brianza, Italy
e-mail: giorgio.allegato@st.com; lorenzo.corso@st.com

C. Valzasina (✉)
ST Microelectronics, Analog MEMS and Sensors Group, MEMS Technology and Design R&D, Cornaredo, Italy
e-mail: carlo.valzasina@st.com

© Springer Nature Switzerland AG 2022

B. Vigna et al. (eds.), *Silicon Sensors and Actuators*,
https://doi.org/10.1007/978-3-030-80135-9_13

First MEMS gyroscopes for automotive were commercialized in the late 1990s and expanded to consumer market in the late 2000s when they found application in smartphones for better user interface and optical image stabilization, gaming, virtual, and augmented reality applications.

During the last years, inertial sensors evolved versus multiaxes integrated systems based on accelerometers and gyroscopes combination (6-axis) or with additional 3-axis magnetometers (9-axis) for fully integrated Inertial Measurement Units (IMUs) [3].

The availability of low-cost sensors and growing market for low-accuracy devices put rapidly MEMS inertial sensors at the top of MEMS device diffusion ranking, a process now called the "MEMS Second Wave" [4].

The development of consumer inertial sensors partially leveraged on the available know-how coming from "First MEMS Wave" of the 1990s but required huge developments in several fields of MEMS design and manufacturing. Inertial MEMS processes were streamlined, and foundries increased wafer size from 4 or 6-inch to 8-inch wafers. Design switched from complex architectures to simpler solutions, exchanging cutting-edge performances with higher yield and shorter time to market. Wafer-to-wafer bonding with hermetic wafer-level encapsulation allowed the transition from ceramic hermetic packages to Systems in Package (SiP) encapsulated with inexpensive, overmolded techniques (Land Grid Array (LGA) or Quad-flat No Leads (QFN) packages being the most common). Testing and calibration process was greatly developed, in close cooperation with test equipment manufacturers, increasing calibration throughput up to the range of thousands of units per hour (UPH).

These technological advances transitioned Inertial MEMS Sensors industry from jewel-like manufacturing to low-cost, high-volume, high-yield processes.

In the context of MEMS inertial sensors expansion, STMicroelectronics was the leader in the MEMS consumerization wave introducing on the market the first high-volume accelerometer for gaming application in the Nintendo WII User Interface in 2006 [5] and introducing the first worldwide integrated 3-axial gyroscope for smartphones in 2010. Today, STMicroelectronics holds a leadership position in the inertial sensor field also in automotive and industrial areas.

In the following paragraphs, accelerometers and gyroscope principles of working will be introduced, and the impact of process parameters on device performances will be presented. The STMicroelectronics "THELMA" technology for the manufacturing of inertial sensors will be presented, and some examples of technology solution to address specific product and application requirements will be described.

13.2 Capacitive MEMS Accelerometers

13.2.1 Accelerometer Working Principles

Accelerometers are sensors used to transduce acceleration (input signal) into electrical output. These sensors could take different naming, depending on the intended acceleration input: Accelerometers are intended to sense the dynamic acceleration

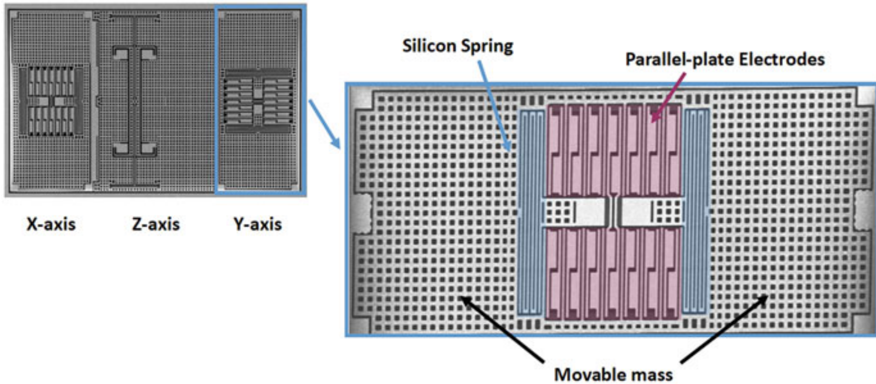

Fig. 13.1 SEM image of MEMS Accelerometer, with highlights on the layout of the movable mass, spring, and electrodes

resulting from motion in an inertial frame of reference, while inclinometers are accelerometers intended to sense the projection of Earth's gravitational field on sense axis. The common measurement unit used to describe accelerometer characteristics is g, corresponding to the freefall acceleration due to Earth's gravitational field at sea level, i.e., (1 g = ~9.81 $\frac{m}{s^2}$).

The most common and widespread MEMS accelerometers are based on capacitive transduction. The structure used to realize a MEMS single-axis accelerometer is a silicon mass suspended via deformable silicon cantilevers [6]. In the presence of external acceleration, the mass is subjected to a force and the thin cantilevers deforms, reaching an equilibrium position. The displacement of the movable mass with respect to the null-force position is transduced into capacitive change with dedicated electrodes.

Detailed description of accelerometer working principles and underlying mathematical models can be found in [7, 8].

An SEM image of a single-axis, surface micromachined MEMS accelerometer realized with STMicroelectronics THELMA process is reported in Fig. 13.1. The perforated silicon plate acts as the inertial mass, while thin polysilicon suspension is used as deformable springs. A set of polysilicon fingers are attached to the movable inertial mass and constitute one plate of the variable capacitor. The other plates are polysilicon-fixed counterelectrodes attached to the substrate with anchoring points (Fig. 13.2).

In Fig. 13.3 is shown the schematic representation of such accelerometer, as well as the transduction chain of the system. We can schematically divide a MEMS capacitive accelerometer into a mechanical part and an electrical transduction part.

The Mechanical model of an accelerometer is usually simplified as one Degree-of-Freedom (DOF) mass-spring-damper system. While this lumped model can be used to describe the main behavior of the microsystem, a more refined model may be used to consider second-order effects such as spurious vibration modes and other nonidealities.

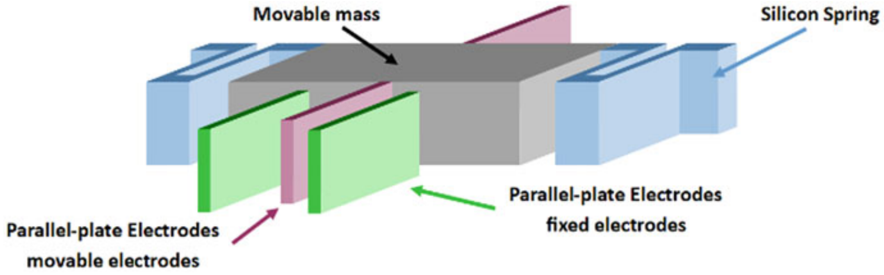

Fig. 13.2 Capacitive MEMS accelerometer schematic

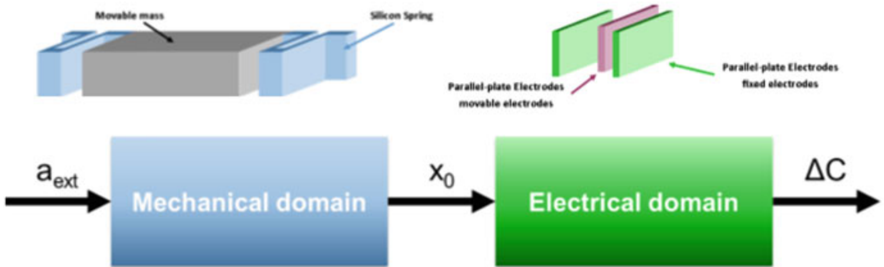

Fig. 13.3 Capacitive MEMS transduction chain

Spring-mass-damper system with one Degree of Freedom (DOF) is shown in Fig. 13.4 and is described by three main parameters: m is the movable mass of the system, b_x is the damping term, and k_x is the elastic stiffness. The general equation of motion is therefore:

$$m\frac{d^2x}{dt^2} + b_x\frac{dx}{dt} + k_x x = ma_{ext} \tag{13.1}$$

where a_{ext} is the external acceleration acting on the system. Solving for the easiest condition of constant acceleration, we find that the equilibrium position of the system is

$$x_0 = \frac{m}{k_x}a_{ext} = \frac{1}{{\omega_0}^2}a_{ext} \tag{13.2}$$

$$\omega_0 = \sqrt{\frac{k_x}{m}} \tag{13.3}$$

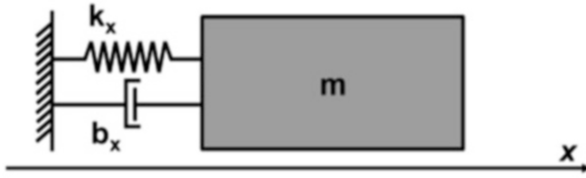

Fig. 13.4 Lumped parameters model of mechanical part of a MEMS accelerometer: the spring-mass-damper system

Where ω_0 is the resonant (angular) frequency of the dynamic system. Equation (13.2) is therefore a measure of low-frequency sensitivity of the mechanical portion of the system in Fig. 13.3.

If input acceleration is not constant, we can treat Eq. (13.1) as a harmonic oscillator, whose solution is of the form

$$x\left(\mathrm{t}\right)=A_1\cos\left(\omega_0 t\right)+A_2\sin\left(\omega_0 t\right) \tag{13.4}$$

where $A_1$and A_2 are constants determined by the initial conditions of the system. The behavior of the system near resonance is dependent on the quantity

$$\xi=\frac{b_x}{2\sqrt{mk_x}} \tag{13.5}$$

known as damping ratio; when ξ is higher than 1, the system is overdamped and input near resonance is quenched, while for $0 < \xi < 1$, the system is underdamped, and resonance peak appears at the resonance frequency. This is of paramount importance when dealing with accelerometer response to external vibration disturbances. The frequency response for different values of the Quality Factor Q ($Q=\frac{1}{2\xi}$) is reported in Fig. 13.5.

Electrical transduction portion of a capacitive MEMS accelerometer is realized with fingers acting as fixed and movable plates of a capacitor. The most common configurations are comb-finger and parallel plate sensing, shown in Fig. 13.6.

Comb-finger sensing is based on the sliding of capacitor plates at fixed gap, and the change in capacitance is achieved with the change of the facing surface area. This method offers the advantage of good linearity for large displacements but suffers from lower sensitivity per unit of rest capacitance C_0. Basic expression for rest capacitance $C_0$and linear sensitivity $\frac{dC}{dx}$of comb-finger is reported in Eq. (13.6)

$$C_0=\varepsilon_0\frac{W\,L_0}{g};\;\frac{dC}{dx}=\frac{d}{dx}\left(\varepsilon_0\frac{W\,L(x)}{g}\right)=\varepsilon_0\frac{W}{g} \tag{13.6}$$

Parallel plate sensing is instead based on changes of the gap between electrodes, at fixed facing area. This sensing configuration has the advantage of increased sensitivity per unit of rest capacitance C_0 with respect to comb-finger, but has the

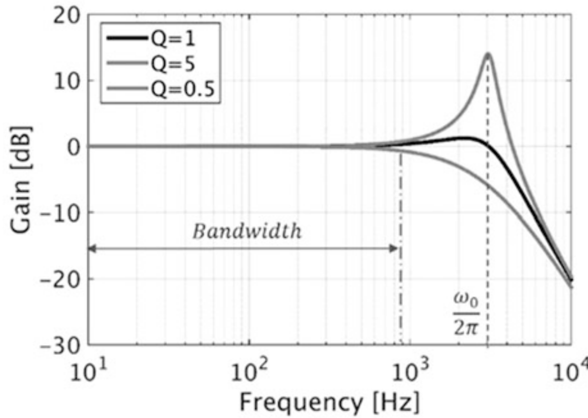

Fig. 13.5 Frequency response of spring-mass-damper system for different Quality factors – ξ. With low Q factor, the frequency response is overdamped and no amplitude amplification is present; with high Q factor, the frequency response is underdamped and resonance peak is visible at resonance frequency

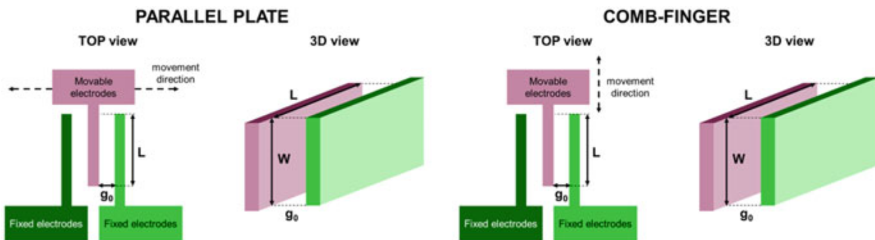

Fig. 13.6 Parallel plates vs. comb finger sensing electrodes for capacitive MEMS

drawback of nonlinear capacitance-displacement response, as can be seen from Eq. (13.7)

$$C_0 = \varepsilon_0 \frac{W\ L}{g_0};\ \frac{dC}{dx} = \frac{d}{dx}\left(\varepsilon_0 \frac{W\ L}{(g-x)}\right) = -\varepsilon_0 \frac{W\ L}{(g-x)^2} \sim -\varepsilon_0 \frac{W\ L}{{g_0}^2} \tag{13.7}$$

We can derive the complete MEMS accelerometer sensitivity to external acceleration in case of parallel plate sensing, for the sensing chain described in Fig. 13.2, we can combine Eqs. (13.7) and (13.2) to get

$$\frac{\Delta C}{\Delta a_{ext}} = C_1 - C_2 = 2\frac{1}{{\omega_0}^2}\varepsilon_0 \frac{W\ L}{{g_0}^2} \tag{13.8}$$

where the equation considers a typical differential configuration of sense electrodes but neglects the readout biasing effect, known as electrostatic spring softening.

In parallel plates' structures, the gap between plates is varied, and therefore the electrostatic force acting on opposite plates will be dependent on position. The electrostatic force directed along the x axis has a magnitude:

$$F = \frac{1}{2}\frac{dC}{dx}V^2 = \frac{1}{2}\frac{\varepsilon A}{(g_0 - \mathrm{x})^2}V^2 \tag{13.9}$$

The dependency of the force to position is crucial as it acts as elastic negative stiffness and changes the actual stiffness of the mechanical spring adding a term:

$$k_{el} = -\varepsilon_0\frac{WL}{g^3}V^2 \tag{13.10}$$

This negative electrostatic stiffness is opposed to the spring elastic stiffness. When the voltage is increased over the value $V_{pull-in}$:

$$V_{pull-in} = \sqrt{\frac{8kg_0{}^3}{27\varepsilon_0 A}} \tag{13.11}$$

The electrostatic stiffness overcomes the elastic stiffness k, and the plates collapse in the so-called pull-in effect.

13.2.2 Accelerometer Specifications and Requirements

When describing inertial sensor performances, the correct option is to refer to the IEEE Standard for Inertial Sensor Terminology 528–2019 [9], in which all useful terms are specified.

When comparing accelerometer datasheets, however, terms may vary from different vendors, requiring some effort to compare different products.

Depending on the application, requirements for MEMS accelerometer may vary significantly; as an example, Zero-Offset value and its drift over external conditions (i.e., temperature, lifetime, etc.) are of critical importance for inclinometers, while its value is almost negligible for automotive-safety high-g accelerometers for airbag firing.

It is therefore of little sense to compare accelerometer intended for different application in a single table to looking for the best performer; in Table 13.1 is nevertheless given a broad picture of how requirement for MEMS accelerometer varies over different applications.

Table 13.1 MEMS accelerometers requirements for different applications

	Consumer user interface	Automotive ESP	Structural health monitoring inclinometer	Automotive airbag firing
Input-range [g]	2–16	6–20	0.25–1	120–400
Zero-offset [mg]	60–120	50	2–5	1000
Zero-offset vs. T [mg/K]	0.5–2.0	0.1–0.3	0.05	50
Noise [$\mu g/\sqrt{Hz}$]	100	–	20	–
Bandwidth [Hz]	100	60	5	400
Power consumption [mW]	0.5	5	2	2

13.2.3 MEMS Accelerometers Design Principles

During the design phase of a MEMS accelerometer, several aspects should be considered: MEMS design always turns out to be a co-design of mechanical transducer, signal conditioning ASIC, and Package.

The basic input parameters for accelerometer design are related to sensor requirements, as well as ASIC parameters and general requirements. Typical examples of such requirements are:

- *Application Requirements*: Full Scale, Resolution or Noise, Input Signal Bandwidth, Zero-Offset stability, Scale Factor stability, linearity, etc.
- *Mission Profile*: operating environmental conditions (temperature, humidity, etc.), vibration and shock levels (operative and maximum survival), expected lifetime, etc.
- *ASIC characteristics*: Readout voltages, capacitance change per unit acceleration.
- *General Requirements*: Sensor Size, Target Cost, etc.

Starting from these requirements, a feasibility study is performed to sketch the basic sensor structure and provide a first-round estimation of MEMS electromechanical performance parameters.

One important tradeoff during the design phase of capacitive accelerometers is represented by the conflicting requirements of increasing as much as possible the mechanical sensitivity of the transducer vs. the full scale and robustness of the sensor.

By maximizing the mechanical sensitivity, i.e., increasing the displacement of the movable mass at reference input acceleration, the transducer reaches lower noise levels and better stability.

In fact, most of the external disturbances such as packaging and soldering stresses, temperature-related stresses, etc. could be modeled as fixed amount of imposed displacement on the transducer movable mass. A high displacement per unit input acceleration will result in a lower input-related effect of the external disturbance.

The high mechanical sensitivity is usually achieved with low frequency of the spring-mass-damper equivalent system, as can be seen from Eq. (13.2). Typical frequencies for consumer MEMS capacitive accelerometers are in the range of few kHz.

With an open-loop readout architecture, movable mass displacement per unit input acceleration is closely related to full scale, i.e., maximum acceleration input allowed before touching stoppers or having pull-in effects. Lower the frequency, lower the full-scale achievable.

A lower resonant frequency for the transducer is also related to lower stiffness of the spring or higher mass, as can be seen from Eq. (13.3). If the system has lower spring stiffness, the mechanical restoring force will be consequently lower, resulting in lower safety margin against stiction. The resonant frequency can be lowered by increasing movable mass and keeping high spring stiffness, at the expenses of transducer dimensions.

Some of the tradeoffs described above can be bypassed using more complex architectures, such as closed-loop force-to-rebalance systems [10] or Frequency Modulated readouts [11]. This comes with the drawback of increased system complexity and increased power consumption.

The design phase aims at predicting sensor performances in all possible process combinations; therefore, not only the typical sensor parameters should be considered, but also the outcome of different process variations.

To design and evaluate Robust sensor Performances [12], different modeling techniques could be employed. Finite Element Modeling (FEM) and analytical or semianalytical modeling can be used to extract typical values of MEMS parameters (e.g., Resonant frequency, rest capacitance, etc.), and the sensitivity of MEMS performances to process parameters.

As an example, process parameters such as structural Epi-poly Silicon thickness and dimensional loss (CD-loss) due to lithography and silicon etching could impact the resonant frequency of an accelerometer.

FEM modal analysis can be applied to the typical MEMS accelerometer geometry to obtain the frequency of first vibration modes.

In Fig. 13.7 are presented the first two vibration modes of the MEMS accelerometer of Fig.13.1, as obtained from an FEM modal analysis in the simulation software ANSYS.

Figure 13.8 shows how changes in process can affect the cross-section of a spring, and specifically, how CD loss variations can result in different sections of a beam while MEMS structural layer thickness variations can alter the thickness of the spring. Sensor mass is also changed by process variations.

Selected variations to the geometry can be applied in the FEM simulation, considering the variability of the process, and "sensitivity" function of resonance frequency vs. process parameters could be extracted. By performing several FEM simulations in different process corners, it is possible to evaluate how MEMS parameters are affected by process variations.

First Vibration Mode

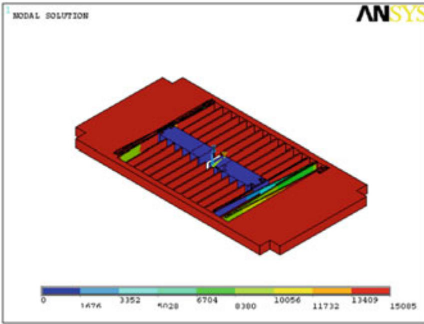

Second Vibration Mode

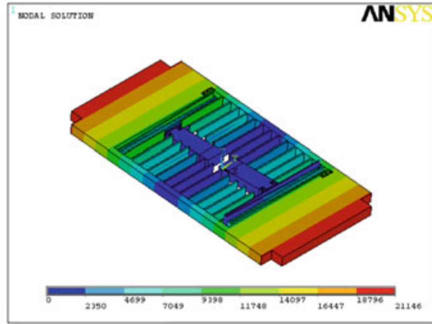

Fig. 13.7 First two vibration modes of the MEMS accelerometer of Fig. 13.1, as obtained from an FEM modal analysis. Color scale represents total displacement in the vibration mode

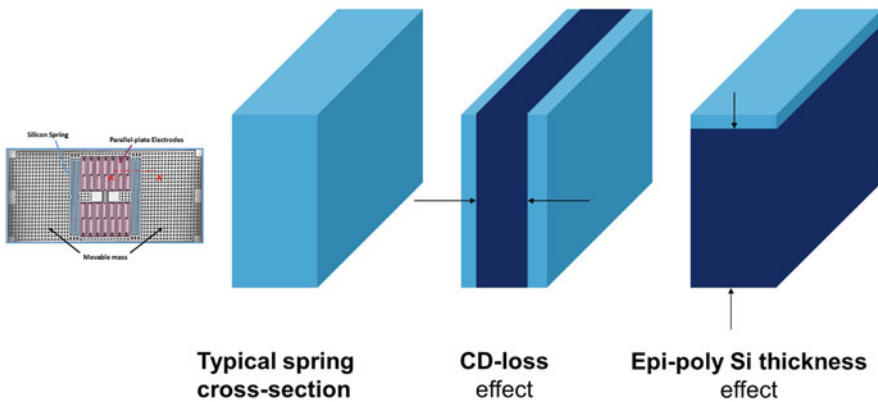

Fig. 13.8 Effects of process on the section of a silicon beam used as a spring: CD loss is the dimensional loss due to Silicon etching process, resulting in reduced beam cross-section; thickness of the beam is influenced by polysilicon growth/removal

Such method is known as *corner analysis* and offers the possibility to investigate MEMS parameter dependency on process variations as well as MEMS performances at the very edges of process specifications (i.e., process corners), while keeping the number of simulations reasonably low. It can therefore be applied to time-consuming simulations such as FEM.

13.3 Capacitive MEMS Gyroscopes

13.3.1 Gyroscope Working Principles

Gyroscopes are sensors capable of converting angular rate (input signal) into electrical output. Angular rate is the amount of angle covered in unit time during a rotation and is measured in degrees per hour [°/h] or degrees per second [dps].

Gyroscopes can be classified as rate gyroscopes, if the measured quantity is angular rate as described before, or Rate-Integrating (angle) gyroscopes, if the physical quantity they measure is the time integral of Angular Rate, i.e., they directly provide the angular change from a specific reference time [13].

Rate-integrating gyroscopes are especially suitable for navigation applications and usually exploit precession of vibration via energy transfer in two vibration modes as the result of external motion [14]. The high symmetry required for these MEMS to operate has prevented them to achieve mass production and commercial success. Rate gyroscopes are instead the most widespread type of MEMS gyroscope in the market.

The principle of operation of rate MEMS gyroscope is the excitation of a vibration mode in response to Coriolis Force acting on a proof mass. Coriolis Force is the apparent force arising in noninertial frame of references as a combination of the linear velocity of the object and the rotation rate of the noninertial frame

$$F_c = -2mv_x \wedge \Omega_{ext} \tag{13.12}$$

Where m is the mass of the moving system, v_x is the linear velocity in one direction, and Ω_{ext} is the external rotation rate.

The basic implementation of a single-axis rate gyroscope is a 2 Degree-of-Freedom (DOF) mechanical system in which one vibration mode (drive axis) is externally excited in resonance and the second vibration mode is excited because of Coriolis Force [15].

The equation of motion for the drive axis x and the sense axis y may be written as:

$$m_x\ddot{x} + c_x\dot{x} + k_x x = F_x \sin(\omega t) \tag{13.13}$$

$$m_y\ddot{y} + c_y\dot{y} + k_y y = F_c = -2m\dot{x}\Omega_z \tag{13.14}$$

where m_x is the mass, c_x is the dissipation coefficient, k_d is the stiffness, and F_x sin (ωt) is the force applied to drive axis x, while m_y is the mass, c_y is the dissipation coefficient, k_y is the stiffness of the sense axis y, and F_c is the Coriolis force acting on the sense axis as a result of a rotation Ω_z around z axis.

When such a configuration is achieved with discrete springs and masses, the system is called Coriolis Vibratory Gyroscope (CVG). More complex implementations

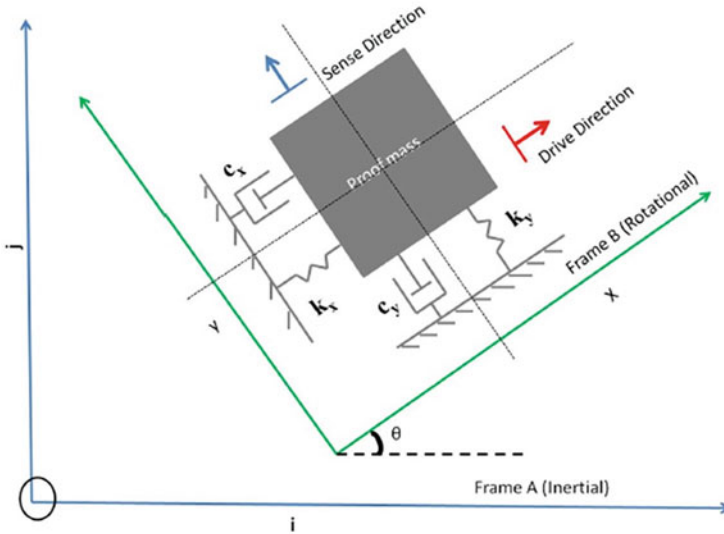

Fig. 13.9 Schematic representation of MEMS Coriolis Vibrating Gyroscope. The mechanical element can be described by 2-Degree-of-Freedom oscillator: a spring-mass-damper system models the drive direction x, and another spring-mass-damper system models the sense direction y. When the frame of reference of the movable mass (x,y) is rotated with respect to an inertial reference (i,j), Coriolis Force couples the drive and sense dynamics

of this 2-DOF mechanical system may rely on solid disks [16] or rings of material [17]. A schematic representation of a Vibrating Coriolis Gyroscope is given in Fig. 13.9.

As for accelerometers, the most widespread principle used for actuation and sensing in MEMS CVG gyroscopes is electrostatic actuation and capacitive sensing.

Electrostatic actuation is the generation of a force in a capacitor because of applied potential on the two armors.

The force acting on a capacitor plate is

$$F_d = \frac{1}{2}\frac{\partial C_d}{\partial x}\Delta V^2 \tag{13.15}$$

where $\frac{\partial C_d}{\partial x}$ is the derivative of the capacitance value along motion direction, and ΔV is the voltage difference between capacitor armors.

In the sense direction, the system can be treated as a capacitive accelerometer where input signal is Coriolis acceleration. Therefore, all the equations described in the previous chapter can be applied.

When dealing with drive and sense axis frequencies, two different configurations are possible:

1. Drive frequency and sense frequency are placed at a fixed distance. The gyroscope is said to operate at mode-mismatched condition.
2. Drive frequency and sense frequency overlap (to a certain amount of accuracy). The gyroscope is said to operate in mode-matched condition.

Mode-matched operation greatly enhances the mechanical sensitivity of the sense axis, due to amplification of sense movement at resonance, but this operation mode requires active frequency steering loops and electromechanical feedback loops to cancel gyroscope nonidealities and drift of mechanical parameters [18].

Practically, most of the MEMS CVG gyroscopes in the market fall in the mode-mismatched operation mode. Sensitivity is not maximized, but a low-power, open-loop sense architecture can be used.

Ideal 2-DOF resonators have completely separated drive and sense mechanical dynamics, but in reality, a coupling may occur. As can be seen in Eqs. (13.15) and (13.16), when a coupling term k_{xy} is introduced in the equations of motion (13.12) and (13.13), the drive x direction and the sense y direction equations are coupled; therefore, a displacement in drive direction will result as a parasitic displacement in y direction and will be displaced as an output signal.

$$m_x\ddot{x} + c_x\dot{x} + k_x x = F_x \sin(\omega t) \tag{13.16}$$

$$m_y\ddot{y} + c_y\dot{y} + k_y y + k_{xy}x = F_c = -2m\dot{x}\Omega_z \tag{13.17}$$

The spurious signal arising from such coupling had a 90° phase difference from Coriolis signal and is therefore called quadrature signal. Coupling coefficient is a consequence of fabrication imperfections, specifically anisotropic silicon etching resulting in nonvertical definition of the flexures, that in turn results in nonideal beam's cross-section [19, 20].

When a drive beam has not vertical etching, the drive electrostatic force applied along the X axis will result in parasitic displacement in the Y direction, as described in Fig. 13.10.

In commercial consumer products, complex MEMS designs are used to achieve three-axis sensitivity. The mechanical element can be described as a 4-DOF oscillator with one vibration mode dedicated to drive and the other three vibration modes dedicated to Coriolis Force sensing along the three orthogonal directions. An example of this structure can be found in Fig. 13.11, showing STMicroelectronics gyroscope used in LSM6DS3 6-axis Inertial Measurement Unit (IMU). The main vibration modes corresponding to drive and sense dynamics are presented in Fig. 13.13.

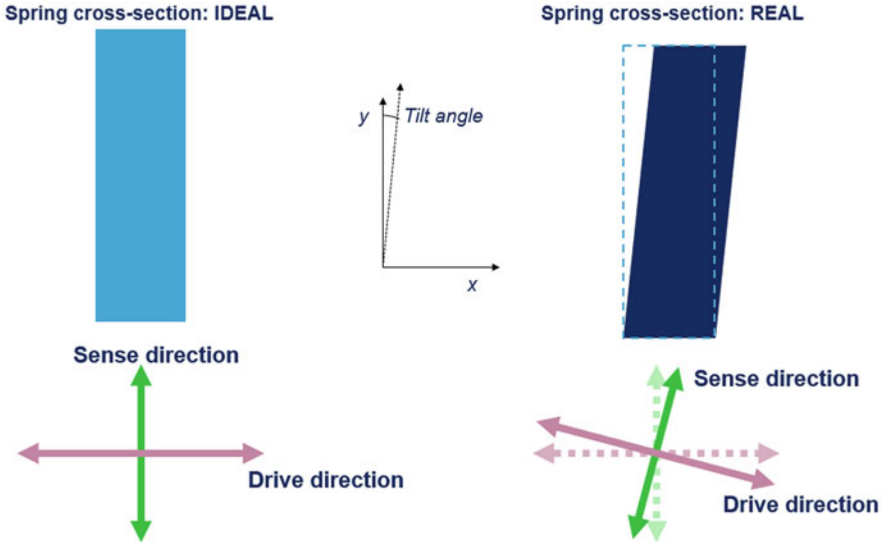

Fig. 13.10 Description of the spring tilt impact on Gyroscope sense/drive displacement

13.3.2 Gyroscope Specifications and Requirements

Performance indicators of MEMS CVG gyroscopes can be found in the IEEE Standard Specification Format Guide and Test Procedure for Coriolis Vibratory Gyros [21], on top of the already mentioned IEEE Standard for Inertial sensors terminology [9].

The main parameters defining MEMS gyroscope performances are:

Bias (Offset or Zero-Rate Level ZRL) is the averaged output of the sensor measured over a specified time in absence of input rotation. Bias is measured in degrees per second [dps] or degrees per hour [$\frac{\circ}{h}$]. ZRL behavior may be described as a function of external conditions, such as acceleration sensitivity, temperature sensitivity, temperature gradient sensitivity, temperature hysteresis, and vibration sensitivity. Bias characteristics are usually described in terms of Allan Variance [22], whose components Angle Random Walk (ARW), Bias Instability (BI), and Rate Random Walk (RRW) are a measure of random bias drift. Allan Variance is a powerful method to identify noise sources in inertial sensors and is computed from gyroscope output by clustering the data at given averaging time, computing the two-sample variance of these clusters and plotting the resulting variance as a function of the averaging time.

Scale factor (Sensitivity) is the ratio of a change in output to a change in the input intended to be measured. It can be measured in [V/dps] for analog-output sensors or in [LSB (Least Significant Bit)/dps] for digital sensors. Different error classes are used to describe deviation from the ideal output characteristic: scale factor error,

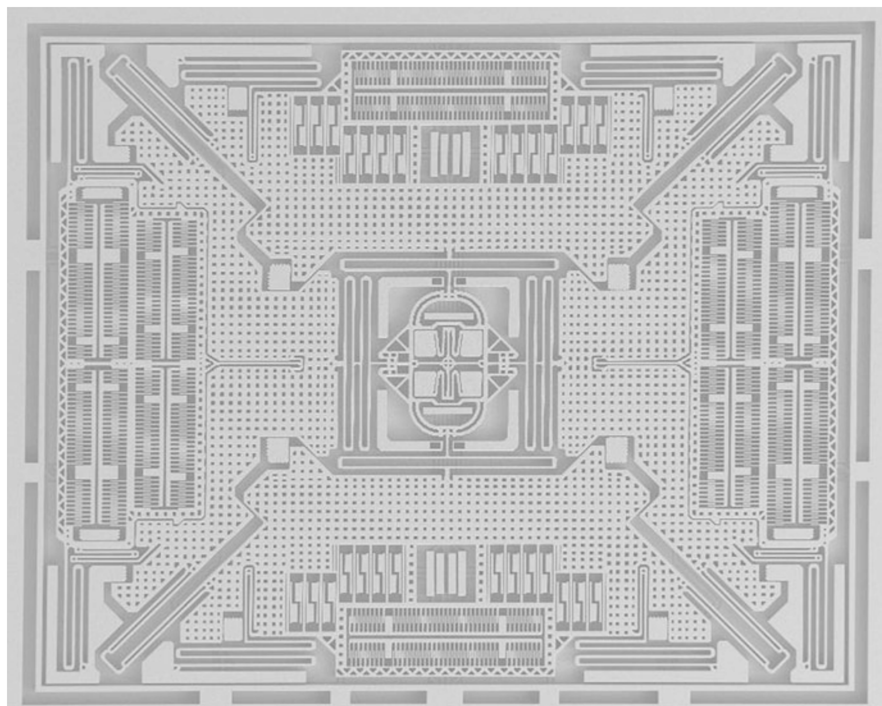

Fig. 13.11 SEM Top View of the LSM6DS3 3-axis gyroscope. Vibration modes of this structure used for drive and sense motion are reported in Fig. 13.13

nonlinearity, asymmetry, and stability against environmental disturbances such as temperature. These deviations from ideal curve are usually measured in [%] or [ppm].

Rate noise density is the spectral density of noise components expressed as [dps/$\sqrt{}$Hz] and refers to the high-frequency noise terms characterized by a white-noise spectrum on the gyro rate output due to correlation time much shorter than the sample time. Noise density has a connection with ARW, and it can be derived from on Allan Variance plot by reading the slope line at T = 1.

Power consumption is the power dissipated by the gyroscope system (MEMS and the control electronics) and is measured in [W]. For low-power devices, the common way to report power consumption is to provide the current drained from power supply during operation in [μA] (Fig. 13.12).

In Table 13.2 are reported typical values of gyroscope performance parameters as a function of the intended application; as can be seen, the typical values of bias stability and scale factor accuracy span several orders of magnitudes. Commercial MEMS gyroscopes are widely diffused in consumer and industrial applications stretching to low-end tactical, while other gyroscope technologies are used for higher accuracy applications (Table 13.3).

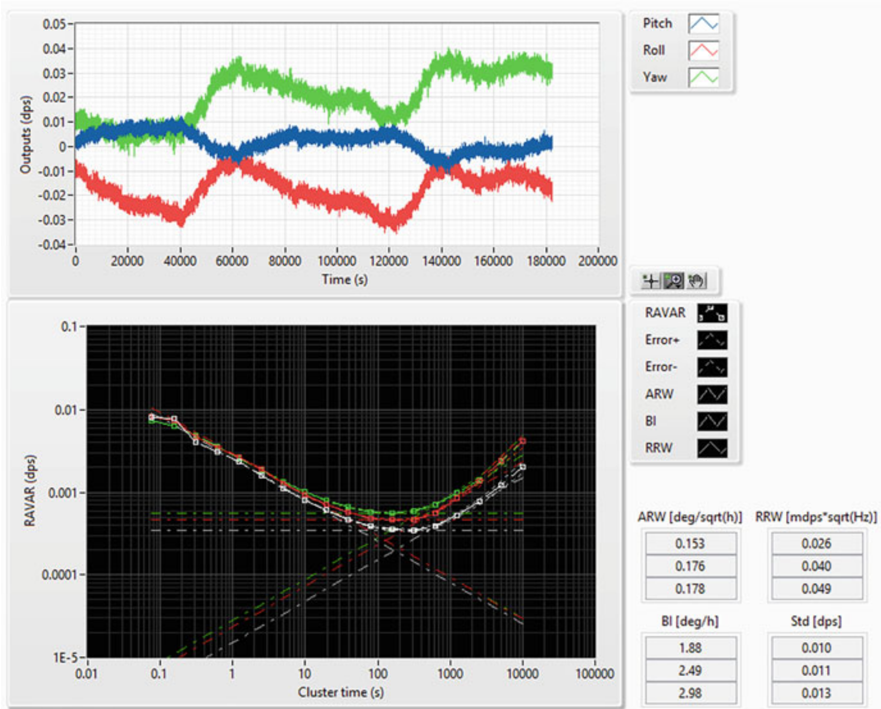

Fig. 13.12 Allan Variance plot. Allan Variance is a measure of stability due to random errors and is used to highlight different noise components in sensors. On the top a series of samples of gyroscope output (with no rate input provided) is reported. The same dataset is analyzed with Allan Variance method in the plot below. This plot is divided in three main regions: the $-1/2$ slope region is a measure of Angular Random Walk AWR (White Noise), the flat region is a measure of Bias Instability (Flicker Noise, or $\frac{1}{f}$), and the $+1/2$ slope region is a measure of Rate Random Walk RRW (Red Noise, or $\frac{1}{f^2}$)

13.3.3 MEMS Gyroscopes Design Principles

The design principles and tradeoffs of MEMS gyroscopes are like the ones of MEMS accelerometers described in the previous chapter. For gyroscopes also, several aspects should be considered and MEMS design is in practice a co-design of technological process, mechanical transducer, signal conditioning ASIC, and package.

The design always starts from sensor requirements and ASIC parameters. The choice of system architecture (how to cancel nonidealities, how to drive the transducer and to read out Coriolis signal, where to set drive and sense resonances, etc.) is fundamental and directly derives from the stability, power consumption, and size requirements.

Table 13.2 Classification of gyroscopes with respect to application

Grade	Application	Bias stability $\left[\frac{\circ}{h}\right]$	Scale factor accuracy [ppm]
Consumer	User interface	30–1000	5000–10,000
Industrial and low-end tactical	Guided ammunitions	1–30	100–5000
Tactical	Platform stabilization	0.1–30	10–100
High-end tactical	Missile navigation	0.1–1	1–10
Navigation	Aerospace inertial navigation	0.01–0.1	<1
Strategic	Submarine navigation	0.0001–0.01	<1

Table 13.3 Reports the typical parameters for consumer and automotive MEMS gyroscopes

	Consumer user interface	Automotive ESP
Input-range [dps]	2000–4000	125–300
Zero-rate level ZRL [dps]	10	2
ZRL vs. T [dps/K]	0.02	0.005
Noise [dps/$\sqrt{}$Hz]	0.007	0.005
Bandwidth [Hz]	400	60
Power consumption [mW]	1	30

With a preliminary feasibility study, it is possible to translate basic sensor parameters (mass, frequencies, capacitance, etc.) into preliminary estimation of MEMS electromechanical performance parameters.

Usually, the architecture of choice for consumer MEMS gyroscopes is closed loop sensing, open loop driving, and electronic open-loop quadrature compensations, a very simple architecture that can achieve reasonably good noise and stability performances with superior power consumption figures.

For automotive Electronic Stability Program (ESP) gyroscopes, the stability requirements are tighter than for consumer counterparts; therefore, usually a closed-loop electromechanical quadrature compensation architecture is used.

Most of the existing MEMS CVG gyroscopes are operated in mode-mismatched, with drive-to sense frequency separation of approximately 5%. The choice of frequency separation, or frequency mismatch, is a critical choice because it defines the tradeoff between gyroscope stability vs. electromechanical sensitivity.

Reducing the frequency mismatch, the mechanical sensitivity is maximized, because Coriolis Force, which is modulated at drive frequency, excites the sense vibration mode in a region closer to resonance. The drawback is that sense transfer function has a steeper phase variation close to sense resonance; therefore, the

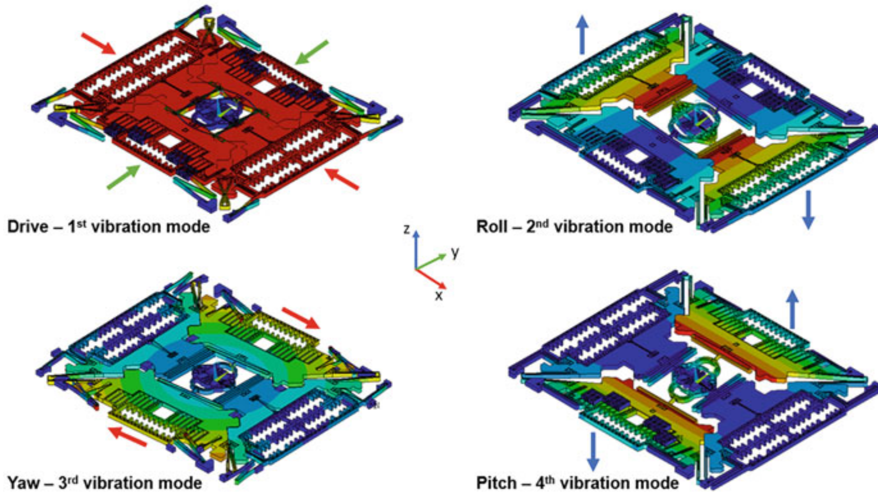

Fig. 13.13 First four vibration modes of a MEMS three-axial gyroscope of Fig. 13.11. These vibration modes are obtained with FEM modal analysis and show Drive Mode, actuated in closed loop with electrostatic force, and Roll, Yaw and Pitch modes, forced by Coriolis force when the gyroscope rotates around *y*, *z*, and *x* axes

coherent demodulation used to separate Coriolis and quadrature signal is affected by larger errors because of environmental disturbances. This in turns translates into larger quadrature signal leakage to Coriolis signal and therefore larger bias drifts, as explained in [23].

This tradeoff could be overcome with usage of closed-loop electromechanical quadrature compensation, that drastically reduces the quadrature signal at MEMS output and therefore reduces the requirement of perfectly coherent demodulation. Electromechanical steering of sense motion to reduce quadrature with dedicated electrodes is well known and widespread used method to improve gyroscope stability, at the price of higher power consumption, larger mechanical structures, and increased system complexity.

As well as for accelerometer, Frequency Modulated readouts have been proposed for gyroscopes [24] and realized with commercial MEMS technologies [25].

Also, for MEMS gyroscopes, the prediction of sensor performances in all possible process combinations enables the achievement of robust sensor performances.

In Fig. 13.13 are presented the first four vibration modes of a MEMS three-axial gyroscope, as obtained from an FEM modal analysis in ANSYS.

In Table 13.4 is shown how structural Epi-poly Silicon thickness CD-loss process parameters impact the resonant frequency of a gyroscope, and therefore the critical parameter of frequency mismatch. This table is obtained by corner analysis with FEM simulations.

Corner Analysis anyhow does not offer any reliable information on the effective distribution of MEMS parameters and tends to overestimate the importance of

Table 13.4 Impact of CD-loss & Epi-poly Thickness on the resonance frequency of Gyroscope vibration modes

CD_loss [μm]	typ	−3σ	+3σ	typ	Typ
Epi-poly Si thickness [μm]	typ	typ	typ	-3σ	+3σ
1st mode frequency [Hz]	20,000	19,000	21,000	20,000	20,000
2nd mode frequency [Hz]	20,850	19,800	21,890	20,690	21,010
3rd mode frequency [Hz]	20,850	19,980	21,720	20,850	20,850
4th mode frequency [Hz]	20,850	19,830	21,870	20,700	21,000

highly unprobable process configurations. A combination of three independent process parameters at 3-sigma values occurs in approximately one-over ten million devices, and designing a system coping with such unlikely configurations could result in poor efficiency and reduced competitiveness, since we can easily screen this part out from production and reduce the overall burden on system design.

Monte Carlo Analysis is a more efficient way to evaluate the distribution of MEMS parameters but requires knowledge of the process parameter statistical distribution and a huge number of simulations to be useful. A faster method to compute spreads of MEMS parameters is a semianalytical model: Analytical formulas are used to compute values of MEMS parameters (sensitivity, frequency, etc.); process spreads are considered by introducing process dependencies in analytical formulations derived from selected FEM and corner analysis.

Figure 13.14 shows the Monte Carlo distribution of the frequency mismatch parameter for the gyroscope described before. As can be seen comparing Fig. 13.14 with Table 13.4, the frequency values obtained with corner analysis represents extreme cases if compared with Monte Carlo simulation. Monte Carlo analysis in fact predicts the full distribution of frequency difference between first Drive mode and second Roll mode, while corner analysis in Table 13.4 only gives point predictions for the different values of frequency in extreme process conditions.

It should be now clear the critical role that process variations have on the design of robust MEMS sensors. It is therefore of paramount importance to adjust MEMS process and MEMS design to achieve target parameters in all process conditions, in a Process-Product Co-Design.

13.4 THELMA Technology Introduction

THELMA is the ST-proprietary technology for the manufacturing of inertial sensors, i.e., accelerometers and gyroscopes. THELMA is an acronym for "**TH**ick **E**pitaxial **L**ayer for **M**icro-gyroscopes and **A**ccelerometers". THELMA technology architecture is based on a surface micromachining process in which a thick epitaxial polysilicon film is used as the structural layer and an oxide film as the sacrificial layer. THELMA technology allows to manufacture micromechanical components which detect movements like acceleration or rotation and translate them into an

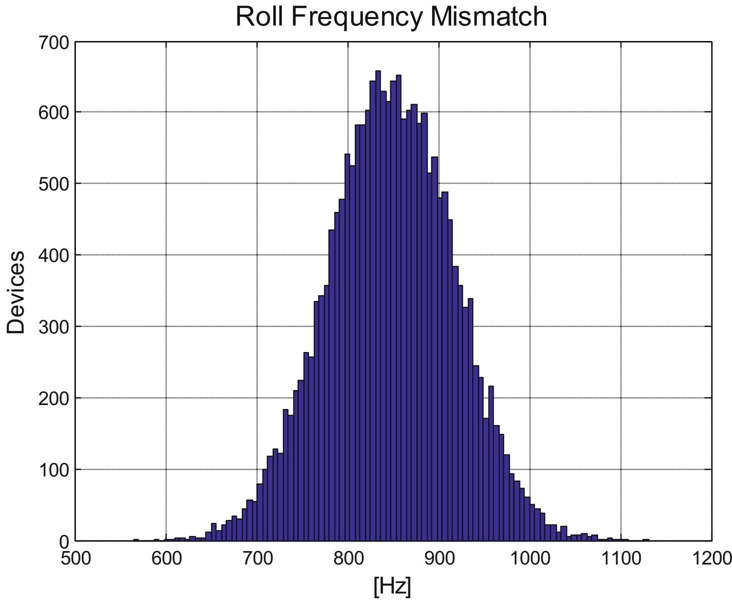

Fig. 13.14 Results of Monte Carlo simulation of frequency difference between first Drive mode and second Roll mode of the gyroscope reported in Fig. 13.11 and whose vibration modes are reported in Fig. 13.13. First, a semianalytical model of the two vibration frequencies is built, highlighting the impact of process parameters in the two frequencies. Then a random set of process parameters is given as input for the model, and the resulting frequency distribution for the two modes is computed. The distribution shown here is the sample-by-sample difference of the two frequency distributions

electrical signal which is read and translated into an analog or digital signal, by an external application-specific IC (ASIC).

As discussed in the previous paragraphs, THELMA sensing principle is capacitive, and it's based on the gap change between moveable and fixed electrodes induced by both in-plane and out-of-plane movements. The key device layers which enable this sensing mechanism are:

– Thick epitaxial polysilicon layer: The film thickness can range from 15 to 60 μm. This layer is patterned by a dry etch process to design the device components like the seismic mass, springs, and in-plane electrodes. Displacement between fixed and moveable electrodes translates into a capacitance change which allows the detection of in-plane movements (Fig. 13.2).
– Buried polysilicon layer: This film is used to design electrical interconnects and buried electrodes below the seismic mass. Out-of-plane displacement of the seismic mass can be detected by a capacitive change between the seismic mass itself and the buried electrodes. Figure 13.15 shows a schematic picture of an out-of-plane capacitor and the principle of out-of-plane capacitive signal reading: The rotation of the inertial mass along an in-plane axis, under an external

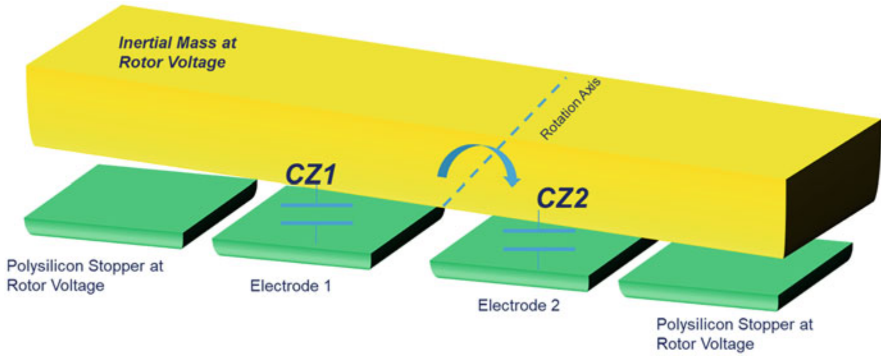

Fig. 13.15 Out-of-plane sensing principle: Inertial mass rotation around an in-plane axis under z-acceleration induces a change on the capacitance of the out-of-plane electrodes (CZ1 and CZ2)

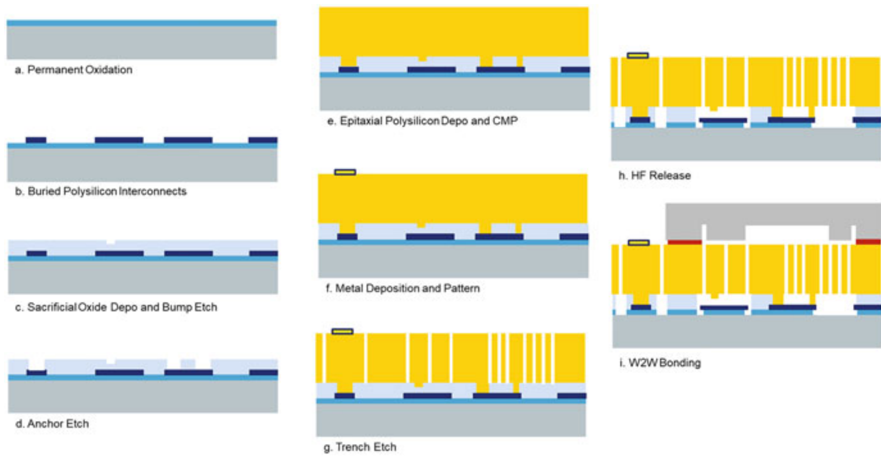

Fig. 13.16 THELMA process flow

acceleration along the z direction, induces a gap change between epitaxial polysilicon and buried polysilicon electrodes.

– A sacrificial oxide layer: This film defines the vertical gap between the buried polysilicon film and the epitaxial polysilicon film of the seismic mass. The oxide layer is removed by a vapor HF process in the areas where the seismic mass must be released and can move under external acceleration or rotation.

A more detailed description of the THELMA manufacturing flow is reported in Fig. 13.16 and described hereafter.

THELMA sensors are manufactured on silicon substrates. The first process step is the realization of a permanent oxide layer (13.16a) to insulate the buried polysilicon layer from the substrate. After permanent oxidation, the buried polysilicon is deposited by LPCVD and patterned to design interconnects and electrodes for

out-of-plane sensing structures (step 13.16b). A TEOS sacrificial layer is deposited afterward; this layer thickness defines the z gap between the epitaxial polysilicon used for the seismic mass and the buried polysilicon. To realize out-of-plane stoppers for the seismic mass and to limit its displacement after release and during device functioning, the sacrificial layer is partially etched to design "molds" for the following epitaxial polysilicon layer (step 13.16c); these "molds", filled by the epitaxial polysilicon, will result into bump structures protruding from the seismic mass backside.

After bump molds formation, the sacrificial layer is patterned to design anchors between the epitaxial polysilicon and buried polysilicon (step 13.16d): These anchors work both as electrical contacts between the two layers and as mechanical anchors to keep the seismic mass anchored on specific poly areas after the final MEMS release process.

Following sacrificial layer patterning, structural epitaxial polysilicon film is deposited and planarized by a chemical mechanical polishing (CMP) process step (step 13.16e). Final structural layer thickness depends on product requirements; THELMA technology implements epitaxial polysilicon thickness values from 15 to 30 μm for consumer and automotive products and up to 60 μm for specific high-end applications where high-sensitivity values are required. This last technology option, known as THELMA-60, will be discussed in the following paragraphs.

An aluminum metal layer is deposited on the epitaxial polysilicon film to design pads for device probing and wire bonding. After metal definition (step 13.16f), the MEMS structural layer is patterned by DRY etch to design device components (step 13.16g): the seismic mass, springs, and in-plane sensing electrodes. The final sensor fabrication step is the release process (13.16h): The sacrificial layer is removed by a vapor HF process, and the device inertial mass is made free to move. To achieve a more effective release process, the seismic mass is patterned with release holes which provide the access to the HF vapors for the sacrificial oxide removal (Fig. 13.17).

To protect the moving components of the inertial sensors during assembly steps and operation and to better control the environment in which the sensors work, THELMA products are packaged at wafer level by a wafer-bonding process. The sensor wafer is bonded to a cap wafer by a glass-frit glue layer, which consists of a low melting temperature glass. Wafer-bonding process is performed under a controlled atmosphere and at a fixed pressure setpoint, which are defined at front-end manufacturing on the wafer bonder equipment.

The cap wafers include through-silicon holes on top of the pads areas which allow the access to metal pads for device testing and wire bonding. Cavities can be designed also on top of the device area with different functions; specific design allows to realize stopper areas to limit the out-of-plane displacements of the seismic mass and to reduce mechanical shocks' impact on device functionality. Containment trenches for glue layer overflow are designed on top cap to prevent glass-frit excess in the device cavity.

Figure 13.18 shows an SEM cross-section of the bonded die.

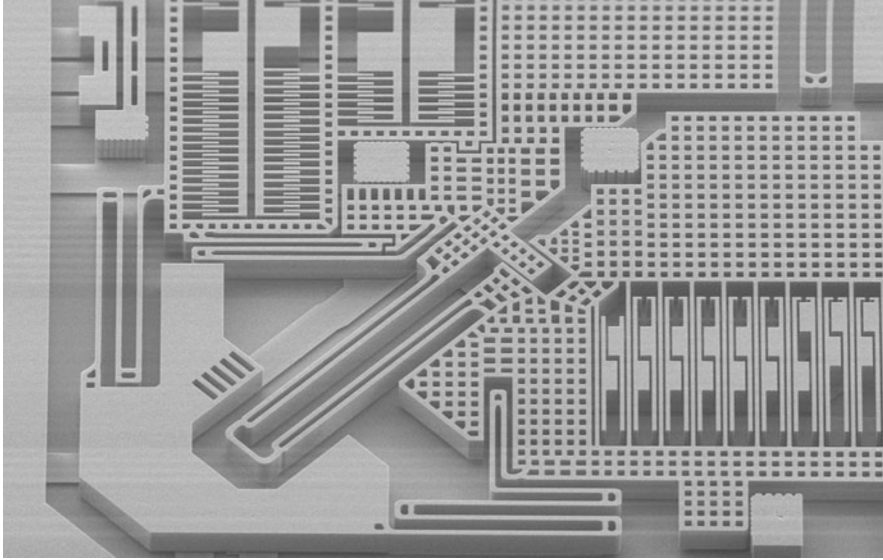

Fig. 13.17 Detail of a THELMA gyroscope with the holed device inertial mass, springs, and electrodes

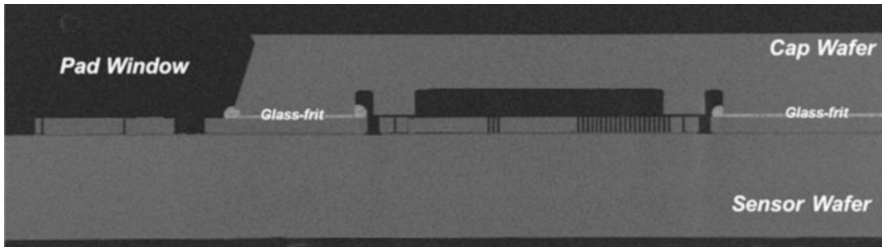

Fig. 13.18 Cross-section View of a MEMS singulated die with pad sensor and cap dice, bonding glue layer, and pad window on the top cap

13.4.1 Process Specificities: Wafer-Level Package (WLP): Vacuum Level through Getter Technology

In gyroscope products, the driving principle is based on the resonating structures electrostatic actuation through parallel plates electrodes. To reduce the mass damping during the driving movement and to keep low actuation voltages and power consumption, wafer bonding at low pressure is required, typically lower than 1 mbar.

To achieve low vacuum levels inside the gyroscope wafer level package, a getter layer [26] is deposited on the cap wafer. The getter layer is a solid material that, if chemically active, can adsorb the reactive gas species from the surrounding environment without desorbing the species themselves during its lifetime. Getter

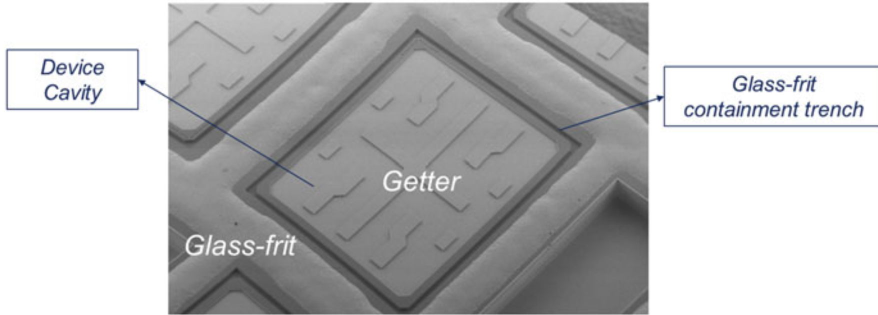

Fig. 13.19 SEM top view of a gyro cap wafer with getter layer inside the device cavity

layers used for MEMS are typically Zr- or Ti-based alloys which are thermally activated, i.e., start to adsorb the environment noninert gas species at temperature higher than an activation threshold. Adsorbed gas species inside the MEMS cavity typically include H2, H_2O, O_2, CO, CO_2, N2, CH4, and more complex hydrocarbons.

Figure 13.19 shows an SEM top view of a gyro cap wafer with glass-frit layer, glass-frit containment trenches, and getter inside the device cavity area. The getter layer is thermally activated during the temperature ramp-up of the wafer-bonding process and absorbs not inert gases which are present in the bonding atmosphere and that can result from surface degassing effects.

By the proper selection of the bonding gas atmosphere with inert (e.g., Ar, Ne, Kr) and not inert gases (e.g., N2, N2H2) in the bond chamber, it's possible to achieve and control low pressure values in the final device cavity. For example, a final device cavity pressure value of 0.1 mbar can be achieved by performing the wafer-bonding process at 10 mbar with a N2 99%/Ar 1% gas mixture. Getter films integration allows also to improve the gyroscope cavity pressure stability. In fact, getter absorbs gas species desorbed from the mems surface ensuring stable pressure inside the bonding cavity during device lifetime and better pressure uniformity from part to part and from run to run.

THELMA platform allows the integration on the same die of an accelerometer and a gyroscope device by a custom bonding layer design and getter integration. These devices are typically named COMBO, since they result from the combination of accelerometers and gyroscopes. On these products, the bonding layer is designed with a double frame to separate gyroscope and accelerometer cavities. Getter deposition is performed in the gyro cavity only to achieve a lower cavity pressure versus the accelerometer one. An SEM top picture of the cap of a COMBO product is shown in Fig. 13.20.

The mechanism which allows to achieve different pressure values in the two device cavities is illustrated in Fig. 13.21. During wafer-to-wafer-bonding process, sensor and cap wafers are put into contact between them; by increasing process temperature, getter is thermally activated, resulting in the absorption of noninert

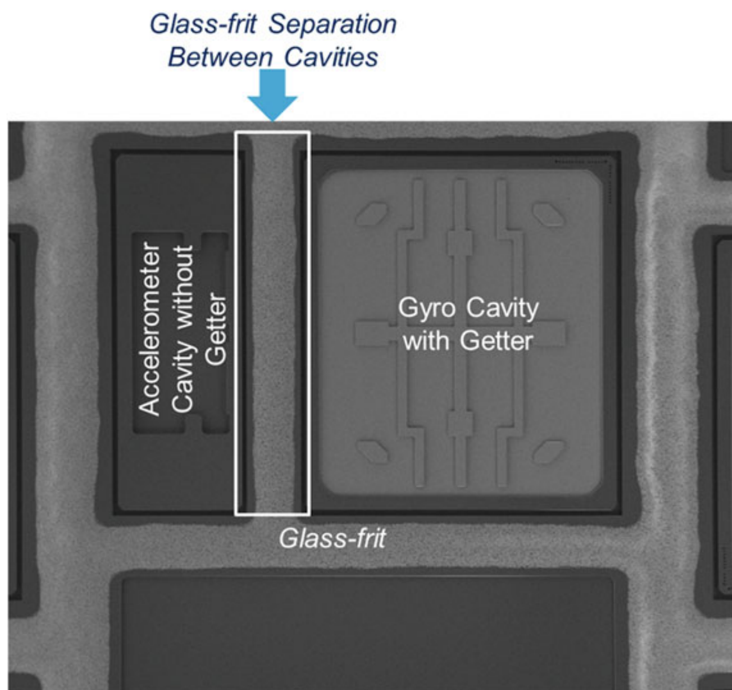

Fig. 13.20 COMBO cap die SEM top view. Accelerometer and gyro cavities are separated by glass-frit; getter is deposited on gyro cavity only

gases present inside the gyro cavity. Due to the glass-frit layer layout which separates the accelerometer and the gyroscope in two different cavities, getter does not absorb noninert gases in the accelerometer cavity and final cavity pressure is defined by the bonding process setpoint. By this approach, it is possible to achieve different pressure values in the two device cavities. For example, by using a bonding gas mix with 1% Ar content, it is possible to keep the accelerometer cavity at a pressure of several tens of mbar versus the gyroscope cavity with a pressure lower than 1 mbar.

This solution allows to keep overdamping on accelerometer side by keeping the benefit of low damping, like low power consumption and low noise, on gyroscope side.

13.4.2 THELMA-60 Technology Platform

THELMA-60 is a process option for the THELMA technology which allows to manufacture inertial sensors with a 60-µm-thick epitaxial polysilicon. A thicker mass has several benefits in terms of performances.

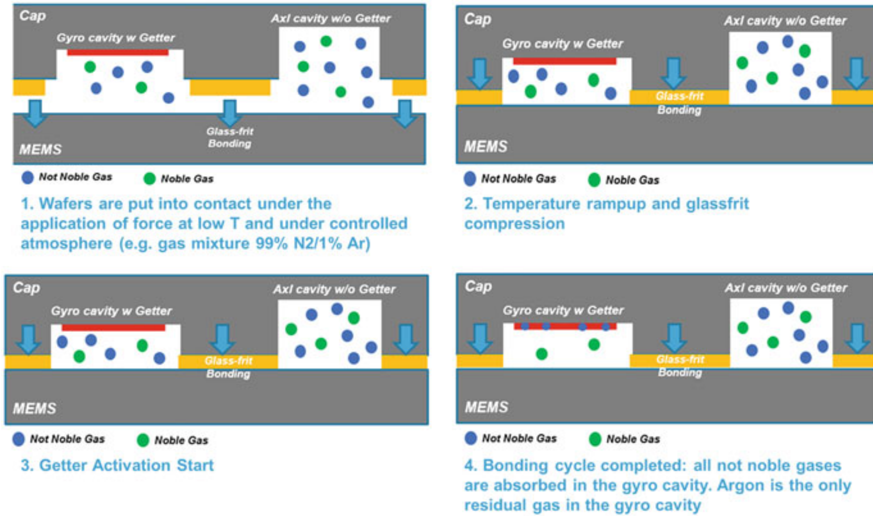

Fig. 13.21 Getter integration description on COMBO product: double pressure cavity approach

A thicker mass allows to realize in-plane capacitors with larger electrodes area which result into a larger capacitance and a higher in-plane sensitivity. THELMA-60 allows to reach sensitivity values in the order of pF/g vs. fF/g values for the traditional THELMA sensors. As an alternative to the increase of sensitivity, a thicker mass allows to put into a smaller area, a device with a specific capacitance value resulting in the shrinkage of the device itself (Fig. 13.22).

The use of a thicker mass allows to also reduce the sensitivity of the device to the Brownian noise, since it is inversely proportional to the sensor mass.

A thicker mass allows the design of out-of-plane sensing devices with larger mass and higher sensitivity. In fact, sensitivity is inversely proportional to the sensor frequency and proportional to the mass of the sensor (Fig. 13.23).

Based on the above considerations, THELMA-60 allows to manufacture high-sensitivity sensors by surface micromachining for applications where complex and expensive bulk micromachining processes were typically used. THELMA-60 bridges the gap between surface and bulk micromachining by enabling the manufacturing of high-end sensors with the benefits of cost effectiveness, flexibility, smaller size, and high yields.

THELMA-60 technology is currently implemented on high-performance applications for medical and industrial market. One example of THELMA-60 application is the manufacturing of high-sensitivity and ultralow-power accelerometers for patient activity monitoring in healthcare applications, like peacemakers and other implantable cardiac devices.

In the industrial field, THELMA-60 technology is used to manufacture sensors for seismic oil and gas exploration. In fact, traditional bulky geophones can be replaced by THELMA-60 products, resulting in better performances, cost effective-

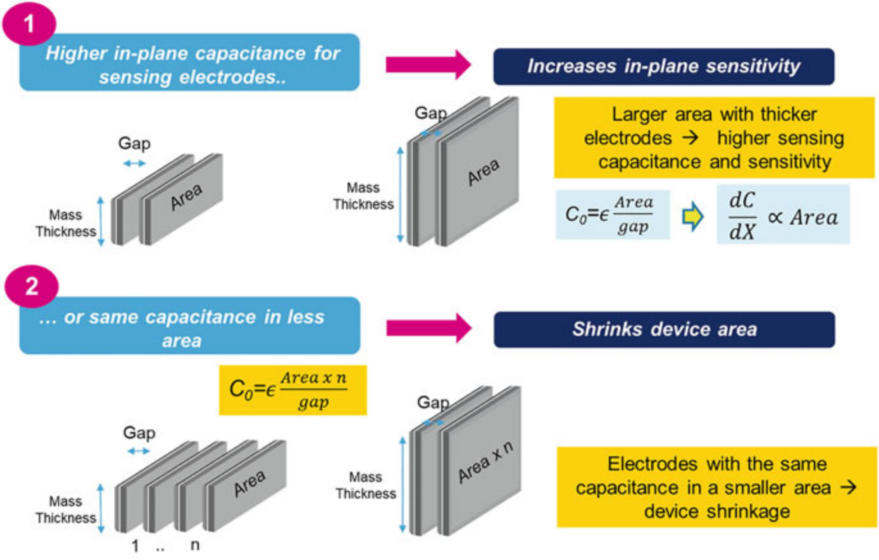

Fig. 13.22 Thicker inertial mass on THELMA-60 allows an increased in-plane sensitivity or the device area shrinkage

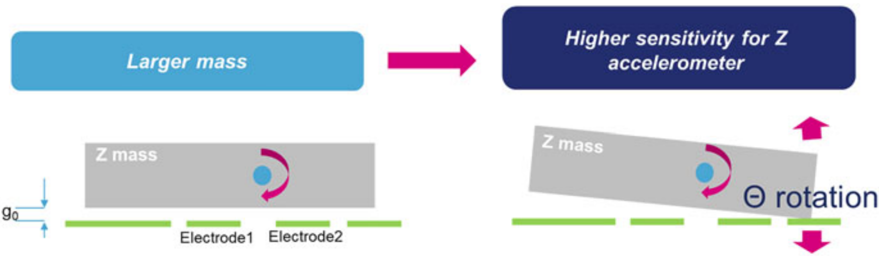

Fig. 13.23 Higher sensitivity is allowed on THELMA-60 for z accelerometers

ness, and space saving. These sensors' working principle is based on the "echo" effect (Fig. 13.24). They are used to detect the vibrations emitted by a source and reflected by the soil and the underlying geological layer to investigate the soil composition and explore gas and soil reservoirs. THELMA geophones exploit THELMA-60 technology benefit and high-vacuum THELMA capability, resulting in high-sensitivity and ultralow noise.

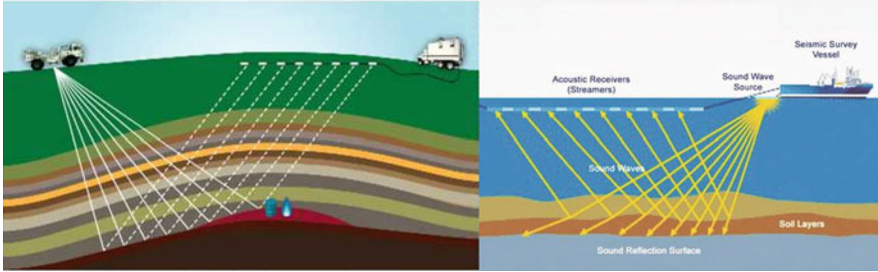

Fig. 13.24 Geophones allow geological exploration by exploiting the echo principle, through the detection of the acoustic reflected waves

13.4.3 THELMA Technology Solutions for MEMS Area Shrinkage

One of the key challenges for sensors in the consumer market is the package area and thickness reduction, which allows integration of these components on smaller portable devices or the integration of more components on the same area. Package area reduction can be achieved by the reduction of the MEMS die area which results also in the increase of the numbers of functional dice present on wafer and a reduction of the single die cost. In this paragraph, some examples of THELMA technology options which allow the die area reduction will be presented.

13.4.3.1 SMERALDO Technology

“SMERALDO” is the Italian translation of the English word “EMERALD”, but also a technology option of the THELMA platform which allows the manufacturing of the final MEMS die without “pad windows” openings, thanks to the integration of through silicon vias. The final aspect of the MEMS die is a full silicon cubic stone but with a valuable device inside, here the name of “SMERALDO” like the precious stone.

In “SMERALDO” technology, the MEMS die area shrinkage is allowed by the removal of a dedicated area for metal pads in the sensor layout: In fact, through silicon vias take the signal from buried polysilicon interconnects to the pads which are placed on the back of sensor die, in the area which is already filled by the glass-frit bond layer on MEMS die area. Figure 13.25 shows a 3D schematic of the SMERALDO MEMS architecture. By this solution, it is possible to achieve a die area shrinkage of 20% by removing the dedicated area device pads, without a significant impact on wafer cost. Figure 13.26 shows a schematics of device layout change and area shrinkage.

“SMERALDO” technology exploits a low-cost process to realize through silicon vias. A schematic TSV process flow description is depicted in Fig. 13.27.

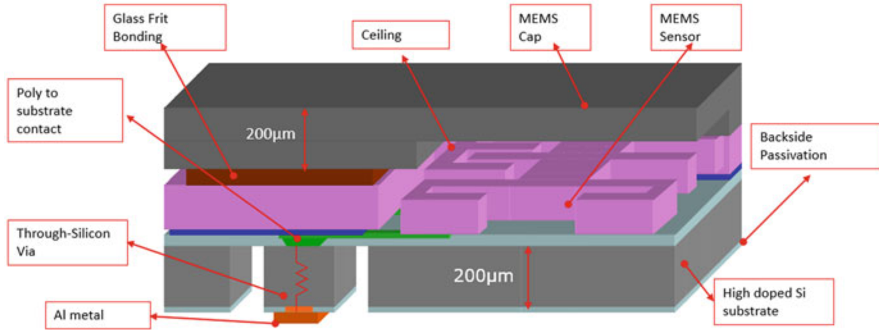

Fig. 13.25 3D schematics of the Smeraldo architecture with thorough substrate silicon via below the glass-frit bond layer

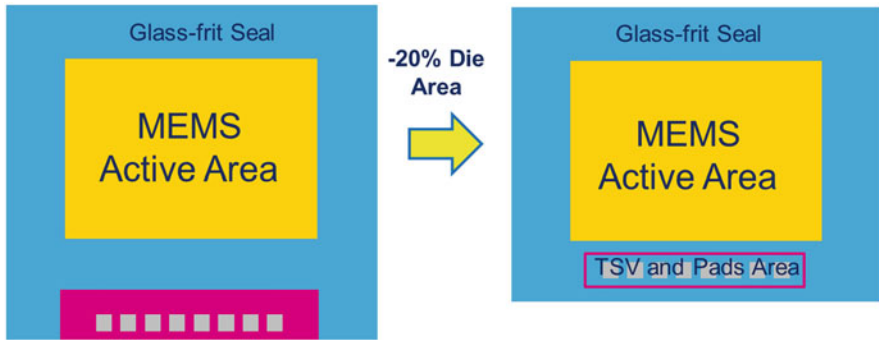

Fig. 13.26 Die area shrinkage by integration of TSV and pads on glass-frit bond seal frame area

The MEMS sensor substrate is a high doped substrate with a resistivity in the order of 1 mohm*cm; signal from MEMS sensor is brought to the substrate by vias opened in the THELMA permanent oxide (13.27a). After glass-frit wafer bonding, the sensor silicon substrate is grinded to a final thickness value of about 200 µm (13.27e), metal for pads is deposited and patterned on sensor substrate backside (13.27f), and silicon "pillars" are patterned by a deep dry etch on areas where poly to substrate vias were designed (13.27g). By this approach, conductive silicon vias that are "pillar-shaped" are fabricated which extract electrical signal from the hermetically sealed device area to the pads placed on the sensor backside.

For MEMS products in LGA package, silicon pillars can be insulated among them by the resin layer which is used for molding during the final LGA package fabrication (Fig. 13.28).

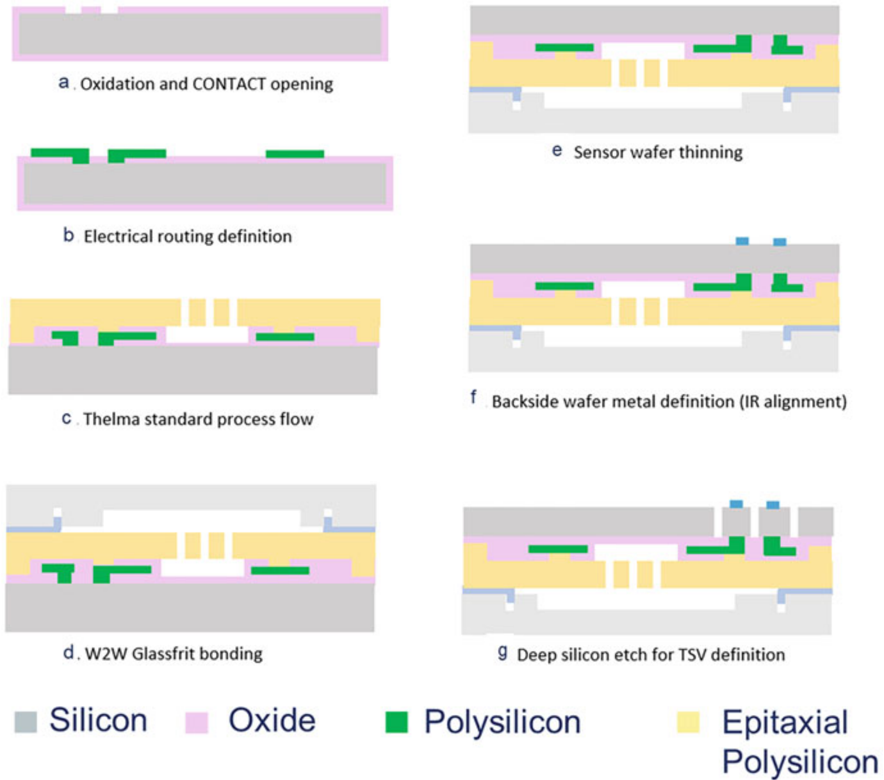

Fig. 13.27 Schematic Smeraldo process flow

13.4.3.2 VIA FIRST Option

THELMA-VIA FIRST is an option of the THELMA process that allows the integration of Via-First Through Silicon Vias (TSV) in the sensor wafer. Unlike the SMERALDO TSVs, whose silicon pillars are surrounded by the molding resin in the device package, THELMA-VIA FIRST TSVs use silicon oxide as dielectric isolation between the vias and the sensor substrate. This approach improves the vias electrical insulation strength and allows the integration of multilevel routing on the back side of the sensor wafer. Figure 13.29 shows the schematic architecture of a MEMS device with TSV realized with this approach.

In THELMA Via First, the MEMS sensor substrate is highly doped with a resistivity in the order of 1 mohm*cm like in the SMERALDO technology option; the electrical signals from the MEMS sensor are brought to the substrate by the contact opened in the THELMA permanent oxide. Via first sensor process flow starts with the vias trenches definition. Electrical isolation between vias and substrate is obtained by vias filling with thermal oxide and undoped polysilicon. A CMP step

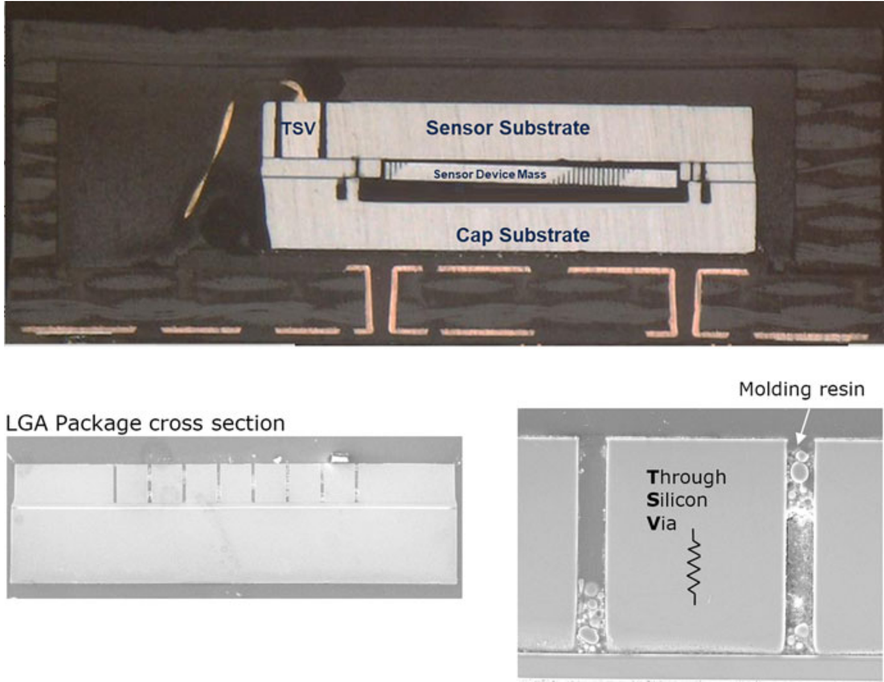

Fig. 13.28 Cross-section of a Smeraldo device in package

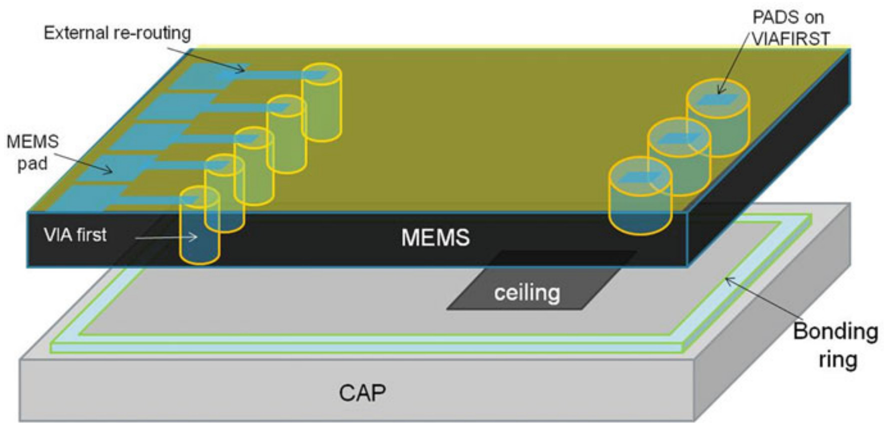

Fig. 13.29 3D schematics of a MEMS device realized with VIA FIRST approach

is then performed to remove polysilicon filling on top of the permanent oxide and provide the right planarity to allow the next steps of sensor flow. Figure 13.30 shows an SEM cross-section of the vias filled with polysilicon and oxide and a detail of the top of the vias with oxide and polysilicon filling.

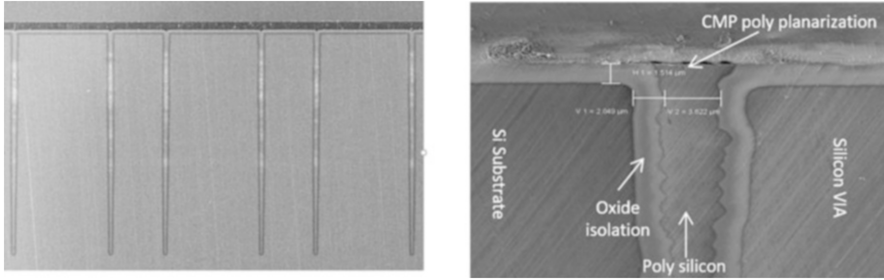

Fig. 13.30 SEM cross-section of VIA FIRST definition on a sensor wafer

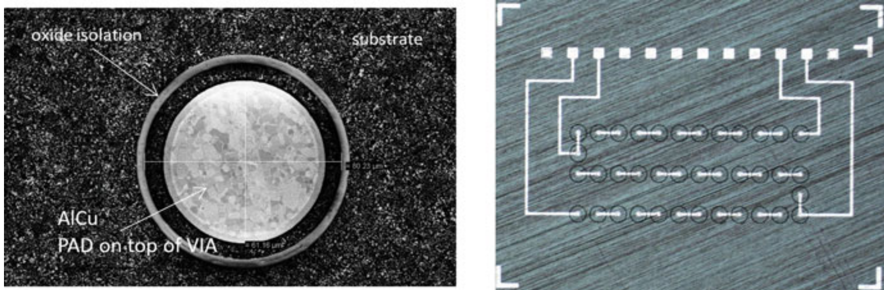

Fig. 13.31 SEM and optical top view of the backside of sensor wafer at the end of the process: a top view of a single via and a structure with multiple interconnected vias are shown

After W2W bonding, the VIAS are revealed through silicon back lapping of the sensor wafer leaving a flat surface that allows further deposition of dielectric and electrical contacts with the external part of the vias. Metal routing can be realized in this phase.

Figure 13.31 shows the finished surface of the sensor wafer after grinding and metal rerouting layer deposition and patterning. A detail of a single via is shown and a daisy chain structured for vias testing where multiple vias are present and metal rerouting layer for vias interconnects among them.

THELMA Via First provides an alternative to THELMA SMERALDO technology for products where device area shrinkage is requested, and a rerouting of the metal layer is requested for package integration requirements.

13.4.3.3 THELMA-PRO: THELMA with PROtective Permanent Oxide Coating

One of the key process steps in THELMA inertial sensor manufacturing is the MEMS release process, in which the sacrificial oxide layer is removed by a vapor HF etch process. During this process, permanent oxide is partially etched below the buried polysilicon interconnects and cause the presence of polysilicon “wings”

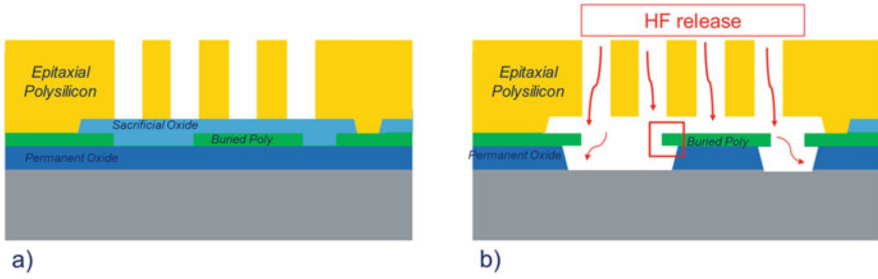

Fig. 13.32 Schematics of a THELMA device before (**a**) and after (**b**) HF MEMS release. Polysilicon wings are red squared in the (**b**) picture

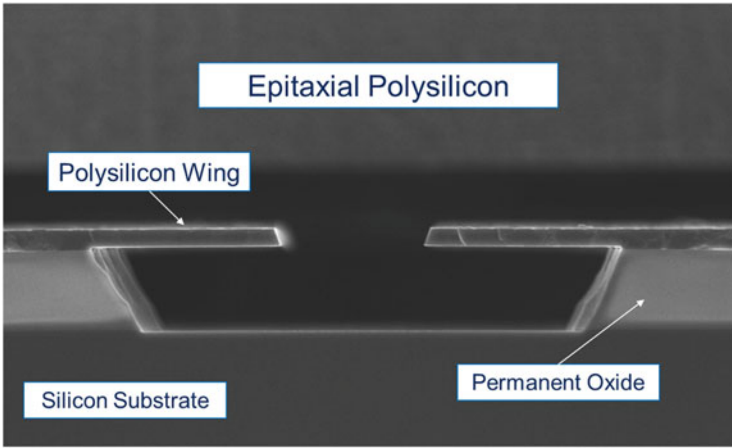

Fig. 13.33 SEM cross-section of polysilicon wings

(Figs. 13.32 and 13.33). These structures represent a potential area of mechanical weakness of the devices, since “wings” breakage can be induced during mechanical shocks in case of sensing mass collision. For this reason, HF vapor etch time must be tightly controlled both to remove completely the sacrificial oxide layer below the inertial mass and to reduce polysilicon “wings” overhang for a robust mechanical structure.

During the product design, the HF release effects on MEMS layers must be considered. In fact, buried polysilicon must be large enough to prevent the interconnected structures to be fragile, typically at least 30 μm. In addition, the release holes density in the epitaxial polysilicon layer must ensure the full removal of the sacrificial oxide layer without inducing a large overhang on polysilicon “wings”; typically, 5 micron distance between neighboring release hole is applied.

The constrains described above translate into a limitation in the device shrinkage both for the space needed to design the buried interconnects and for the lower mass density on the inertial sensor device induced by the high release holes density.

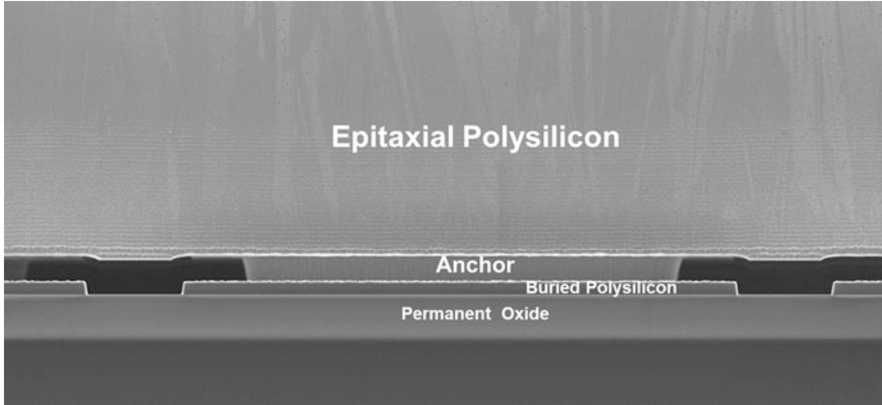

Fig. 13.34 SEM cross-section of a THELMA-PRO device after HF release: no underetch below polysilicon is present

To overcome these limitations and to boost the shrinkage of THELMA MEMS products, a process option of the THELMA technology platform was developed under the name of THELMA-PRO. In this technology, an HF-resistant protective coating layer is deposited on top of the permanent oxide before the polysilicon interconnects deposition. The first result of this layer introduction is the removal of the polysilicon “wings”. Figure 13.34 shows an SEM cross-section of a THELMA-PRO sensor product after HF release.

Due to “wings” removal, polysilicon interconnects width is no more affected by considerations related to the HF release process. In addition, longer HF release steps can be implemented and release holes distance on the inertial mass can be increased, resulting in a higher sensor mass density versus standard THELMA technology. Typically, in THELMA-PRO polysilicon interconnects, width can be reduced to few micron and release holes distance is increased from 2 to 3 times the values used for standard THELMA. Figure 13.35 shows a comparison between the release holes densities of two THELMA and a THELMA-PRO product and the SEM top pictures of two gyroscopes manufactured by these technologies.

The combined effect is a 30% area shrinkage on product die thanks to the reduction of the space required from interconnects and from the inertial mass.

THELMA-PRO technology is currently used in high-volume production on both accelerometers and gyroscopes for consumer, industrial, and automotive markets. Die area shrinkage has been the key driver for THELMA-PRO introduction on consumer products. Polysilicon “wings” removal and the consequent improvement of the device mechanical robustness have been the driver for THELMA-PRO adoption also for the automotive market and in general to those applications where robustness to high-g mechanical shocks is required.

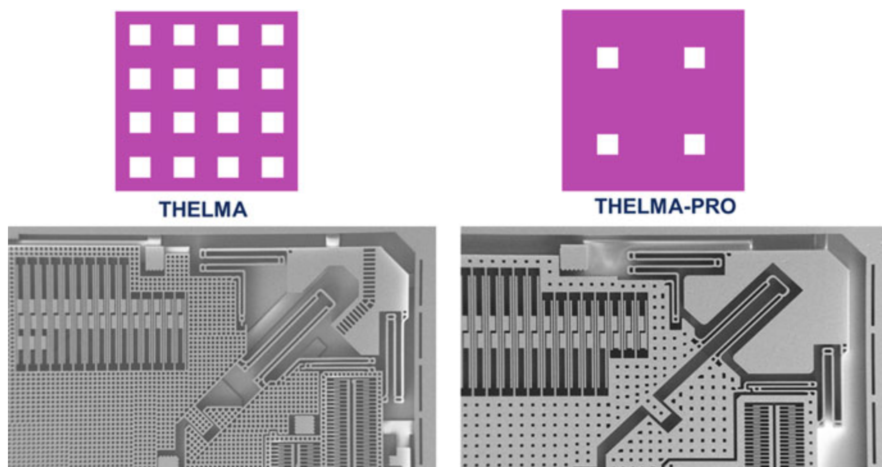

Fig. 13.35 THELMA and THELMA-PRO release hole densities

13.5 Conclusions

Thanks to dedicated MEMS technologies and evolving design principles, MEMS inertial sensors have dramatically improved in the last decade in terms of accuracy, quality and reliability, and cost.

At the beginning of MEMS accelerometer era, MEMS sensors were available only with very limited full-scale, bulky packages and power consumption in the mW region. Nowadays low-power accelerometers for consumer and wearable electronics applications offer state-of-art power consumption in appealing small packages, with good noise and accuracy.

The evolution of MEMS gyroscopes has followed a similar path, increasing the number of available sense axis from 1 to 3 and further decreasing size and power consumption. The further improvements of MEMS gyroscopes will proceed in strong reduction of power consumption to enable low-power applications and further improvement of gyroscope performances to enable high-value applications.

The key recipe for such roadmap is the evolution of technology capability in terms of reduced process variability and improved process architectures toward complete 3D structures, and the parallel evolution of better modeling of physical phenomena at a smaller accuracy scale.

References

1. Roylance, L. M., & Angeli, J. B. (1979, December). A batch-fabricated silicon accelerometer. *IEE Transactions on Electron Devices, ED-26*(12).
2. https://www.analog.com/media/en/technical-documentation/obsolete-data-sheets/2044696ADXL50.pdf

3. Vigna, B. (2011) *Tri-axial MEMS gyroscopes and six degree-of-freedom motion sensors*. In International electronic device meeting.
4. Edwards, C. (2009). *MEMS: The second wave*. E&T – Engineering and Technology. https://eandt.theiet.org/content/articles/2009/07/mems-the-second-wave/, Monday, July 6.
5. https://investors.st.com/news-releases/news-release-details/stmicroelectronics-drives-gaming-revolution-nintendos-wiitm
6. Lemkin, M., & Boser, B. E. (1996). *A micromachined fully differential lateral accelerometer*. In Proceedings of custom integrated circuits conference, San Diego, CA, USA, pp. 315–318.
7. Kempe, V. (2011). *Inertial MEMS: Principles and practice*. Cambridge University Press.
8. Corigliano, A., Ardito, R., Comi, C., Frangi, A., Ghisi, A., & Mariani, S. (2018). *Mechanics of microsystems*. Wiley.
9. 528–2019 – IEEE Standard for Inertial Sensor Terminology. https://standards.ieee.org/content/ieee-standards/en/standard/528-2019.html
10. Lemkin, M. A., Boser, B. E., Auslander, D., & Smith, J. H. (1997). *A 3-axis force balanced accelerometer using a single proof-mass*. In Proceedings of international solid state sensors and actuators conference (Transducers '97), vol. 2, Chicago, IL, USA, pp. 1185–1188. https://doi.org/10.1109/SENSOR.1997.635417.
11. Marra, C. R., Tocchio, A., Rizzini, F., & Langfelder, G. (Oct. 2018). Solving FSR versus offset-drift trade-offs with three-Axis time-switched FM MEMS accelerometer. *Journal of Microelectromechanical Systems, 27*(5), 790–799.
12. Robust sensor Performances.
13. Shkel, A. M. (2006). *Type I and type II micromachined vibratory gyroscopes.* In Proceedings of the IEEE/ION position location navigation symposium, April 2006, pp. 586–593.
14. Meyer, A. D., Rozelle, D. M., Trusov, A. A., & Sakaida, D. K. (2018). *milli-HRG inertial sensor assembly – A reality*. In Proceedings of the IEEE/ION position location navigation symposium, April 2018.
15. Bernstein, J., Cho, S., King, A. T., Kourepenis, A., Maciel, P., & Weinberg, M. (1993). *A micromachined comb-drive tuning fork rate gyroscope.* In Proceedings of the MEMS '93, pp. 143–148.
16. Johari, H., & Ayazi, F. (2006). *Capacitive bulk acoustic wave silicon disk gyroscopes*. In Proceedings of the IEEE electron devices meeting, December 2006, pp. 1–4.
17. Ayazi, F., & Najafi, K. (1998). *Design and fabrication of high-performance polysilicon vibrating ring gyroscope*. In: IEEE MEMS, Heidelberg, Germany, pp. 621–626.
18. Prikhodko, I. P., Gregory, J. A., Clark, W. A., Geen, J. A., Judy, M. W., Ahn, C. H., & Kenny, T. W., *Mode-matched MEMS Coriolis vibratory gyroscopes: Myth or reality?*, In 2016 IEEE/ION Position Location and Navigation Symposium (PLANS), pp. 1–4.
19. Weinberg, M. S., & Kourepenis, A. (2006). *Journal of Microelectromechanical Systems, 15*(3), 479–491.
20. Izadi, M., Braghin, F., Giannini, D., Milani, D., Resta, F., Brunetto, M. F., et al. (2018). *A comprehensive model of beams' anisoelasticity in MEMS gyroscopes, with focus on the effect of axial nonvertical etching*. In 2018 IEEE International Symposium on Inertial Sensors and Systems (INERTIAL).
21. IEEE Standard 1431–2004 (2004). *IEEE standard specification format guide and test procedure for Coriolis Vibratory Gyros*, IEEE Standard 1431–2004.
22. El-Sheimy, N., Hou, H., & Niu, X. (2008). Analysis and modeling of inertial sensors using Allan variance. *IEEE Transactions on Instrumentation and Measurement, 57*(1).
23. Facchinetti, S., Guerinoni, L., Falorni, L. G., Donadel, A., & Valzasina, C. (2017). *Development of a complete model to evaluate the Zero Rate Level drift over temperature in MEMS Coriolis vibrating gyroscopes*. In 2017 IEEE International Symposium on Inertial Sensors and Systems (INERTIAL), March 2017, pp. 125–128.
24. Kline, M., Yeh, Y., Eminoglu, B., Najar, H., Daneman, M., Horsley, D., & Boser, B. (2013, January). *Quadrature FM gyroscope*. In 2013 IEEE 26th international conference on Micro Electro Mechanical Systems (MEMS), pp. 604–608.

25. Minotti, P., Dellea, S., Mussi, G., Bonfanti, A. G., Facchinetti, S., Tocchio, A., et al. High scale-factor stability frequency-modulated MEMS gyroscope: 3-Axis sensor and integrated electronics design. *IEEE Transactions on Industrial Electronics, 65*(6), 5040–5050.
26. Moraja, M., Amiotti, M., & Longoni, G., MST. (2003). *Patterned getter film wafers for wafer level packaging of MEMS*, Munich, October 2003.